The Astrophysical Journal, 798:2 (12pp), 2015 January 1 doi:10.1088/0004-637X/798/1/2

MULTI-FREQUENCY, MULTI-EPOCH STUDY OF Mrk 501: HINTS FOR A TWO-COMPONENT NATURE OF THE EMISSION

A. Shukla[1], V. R. Chitnis[1], B. B. Singh[1], B. S. Acharya[1], G. C. Anupama[2], P. Bhattacharjee[3], R. J. Britto[3,5], K. Mannheim[4], T. P. Prabhu[2], L. Saha[3], and P. R. Vishwanath[2]
[1] Department of High Energy Physics, Tata Institute of Fundamental Research, Mumbai 400005, India
[2] Indian Institute of Astrophysics, II Block, Koramangala, 560 034, Bangalore
[3] Saha Institute of Nuclear Physics, 1/AF, Bidhannagar, 700 064, Kolkata, India
[4] Universität Würzburg, 97074 Würzburg, Germany
Received 2014 March 10; accepted 2014 October 14; published 2014 December 9

ABSTRACT

Since the detection of very high energy (VHE) γ-rays from Mrk 501, its broadband emission of radiation was mostly and quite effectively modeled using the one zone emission scenario. However, broadband spectral and flux variability studies enabled by the multi-wavelength campaigns carried out during the recent years have revealed the rather complex behavior of Mrk 501. The observed emission from Mrk 501 could be due to a complex superposition of multiple emission zones. Moreover, new evidence of detection of very hard intrinsic γ-ray spectra obtained from *Fermi*-LAT observations has challenged the theories about the origin of VHE γ-rays. Our studies based on *Fermi*-LAT data indicate the existence of two separate components in the spectrum, one for low-energy γ-rays and the other for high-energy γ-rays. Using multi-waveband data from several ground- and space-based instruments, in addition to HAGAR data, the spectral energy distribution of Mrk 501 is obtained for various flux states observed during 2011. In the present work, this observed broadband spectral energy distribution is reproduced with a leptonic, multi-zone synchrotron self-Compton (SSC) model.

Key words: BL Lacertae objects: individual (Mrk 501) – galaxies: jets

1. INTRODUCTION

The BL Lac object source Mrk 501 ($z = 0.034$) belongs to a sub-class of active galactic nuclei (AGNs) that are known as high-energy peaked blazars (HBLs). The broadband emission (radio to γ-rays) of these objects is dominated by non-thermal radiation that is produced in the innermost part of the jets, which are oriented very close to our line of sight. This broadband emission is strongly Doppler boosted. Like other TeV blazars, the spectral energy distribution (SED) of Mrk 501 characteristically shows a double-peaked profile. These peaks occur at keV and GeV/TeV energies when the SED is plotted in the νF_ν versus ν representation. The general understanding is that the first hump of the SED is caused by synchrotron radiation from the electron population gyrating in magnetic fields of the jet, but the origin of the GeV/TeV hump is unclear. The composition of these jets is also not known; it is not clear whether they are made of electron–positron plasma or electron–proton plasma. Even though Mrk 501 has been observed over the last two decades in the entire electromagnetic spectrum, the existing multi-frequency data could not provide an explicit answer for the physical mechanisms that are responsible for the production of the GeV/TeV hump. This hump may be produced by the interaction of electrons with photons in leptonic models (Krawczynski 2004; Dermer & Schlickeiser 1993; Ghisellini & Madau 1996) or protons with photon fields or magnetic fields in hadronic models (Aharonian 2000; Mücke et al. 2003; Mannheim 1998) or by a mixed lepto-hadronic scenario (Cerruti et al. 2012).

The multi-frequency correlations and spectral energy distributions of Mrk 501 were studied extensively in the past by Sambruna et al. (2000), Pian et al. (1998), Villata & Raiteri (1999), Krawczynski et al. (2000), Tavecchio et al. (2001), and Ghisellini et al. (2002), but the nature of this object is still far from being understood. The main reasons for this are the moderate sensitivities of the γ-ray instruments and the lack of simultaneous multi-frequency data during long periods.

Since the detection of this source at above 500 GeV by the Whipple observatory (Quinn et al. 1996), it has shown several high states over the entire electromagnetic spectrum and also a few orphan TeV flares (Abdo et al. 2011; Neronov et al. 2012). Mrk 501 is also known for its major, long-timescale and short-timescale flares in X-rays and very high energy (VHE) γ-rays (Catanese et al. 1997; Pian et al. 1998; Xue & Cui 2005; Albert et al. 2007). One of its historical outbursts was observed in 1997 when the flux at energies above 1 TeV reached up to 10 Crab (Aharonian et al. 1999a, 1999b). Following this outburst, the average flux of VHE γ-rays dropped to 0.3 Crab during 1998–1999 (Aharonian et al. 2001).

Rapid, intra-night variability has been displayed by Mrk 501 over the entire electromagnetic spectrum (Gupta et al. 2008; Albert et al. 2007; Gupta et al. 2012). Fast variability over timescales of minutes has been detected during TeV orphan flares, making the study of this object very interesting (Albert et al. 2007). There have been several mechanisms proposed for producing the observed variability in the jet emission, ranging from plasma mechanisms (Krishan & Wiita 1994), beamed radiation (e.g., Crusius-Waetzel & Lesch 1998), coherent instability in a compact emission region (e.g., Begelman et al. 2008), misaligned minijets inside the main jet (e.g., Giannios et al. 2010), jet deceleration (Georganopoulos & Kazanas 2003; Levinson 2007), wiggles in an anisotropic electron beam directed along the jet (Ghisellini et al. 2009), relativistic plasma blob inside the jet (blob-in-jet model; Katarzyński et al. 2001), and plasma

[5] Now at Department of Physics, University of Johannesburg, P.O. Box 524, Auckland Park 2006, South Africa.

instability such as a firehose (Subramanian et al. 2012) caused by an anisotropic electron beam.

Some fundamental questions regarding this source such as the content of its jet, location, and mechanism of γ-ray emission and the origin of observed variability are still not answered unambiguously. In an attempt to improve our understanding of the source, we present a detailed study of multi-waveband data taken during 2011 January to 2012 March using ground- and space-based instruments in this work. We have fitted multi-waveband SEDs with a multi-zone SSC model and discussed constraints on the physical parameters of Mrk 501.

In this paper, we study the multi-wavelength–multi-epoch behavior of Mrk 501 during 2011. Five different flux states at different epochs along with a quiescent state SED observed by Abdo et al. (2011) are modeled with a two-zone SSC scenario and are compared. Multi-wavelength observations and analysis are presented in Section 2, and results are discussed in Section 3. A description of our new two-zone model and the modeling of six different flux states are described in Section 4. Finally, we discuss implications of our two-zone model on the blazar parameters considering Mrk 501 as an example in Section 5.

2. MULTI-WAVELENGTH OBSERVATIONS AND ANALYSIS

VHE γ-rays observations were made using High Altitude GAmma Ray (HAGAR) telescope array, in Hanle, India. In addition, archival data from the Large Area Telescope (LAT) on board *Fermi*; Proportional Counter Array (PCA), and All-Sky Monitor (ASM) on board *RXTE*; X-Ray Telescope (XRT), Ultraviolet/Optical Telescope (UVOT) and Burst Alert Telescope (BAT) on board *Swift*; SPOL; and Owens Valley Radio Observatory (OVRO) were analyzed to obtain light curves and energy spectra.

2.1. Optical and Radio Data

The optical and radio data made available from the *Fermi* multi-wavelength support program are used. The optical observations were made by the SPOL team using the SPOL CCD imaging/spectropolarimeter at Steward Observatory (Smith et al. 2009). The optical *V*-band photometric and polarimetric fluxes are publicly available on Web sites,[6] and these data are used to obtain light curves and SEDs.

The 15 GHz radio observations were made by using a 40 meter single-dish telescope at OVRO. The radio fluxes are also publicly available from the OVRO collaboration on Web sites,[7] and they are used to obtain light curves at radio wavelengths. Details of the analysis method are described in Richards et al. (2011). In addition to this, we have also plotted radio data from the Very Long Baseline Array (VLBA) at frequencies of 5 GHz and 43 GHz and from the Submillimeter Array (SMA) at 230 GHz, obtained from Abdo et al. (2011) on each SED for reference, as we do not have any radio observations of the core during 2011–2012.

2.2. RXTE and Swift

The PCA (Bradt et al. 1993) on board *RXTE* is an array of five identical xenon-filled proportional counter units (PCUs). The PCUs cover an energy range from 2 to 60 keV with a total collecting area of 6500 cm^2. We have analyzed standard 2 PCA data that have a time resolution of 16 s with energy information in 128 channels. Data analysis was performed using HEASOFT (version 6.10). Data from PCA were analyzed to obtain the X-ray energy spectrum and light curve. For each of the observations, data were filtered using the standard procedure provided in the *RXTE* Cook Book. The background models were generated with the tool "pcabackest," based on *RXTE* GOF calibration files for a "faint" source (less than 40 ct/sec/PCU).

The XRT on board *Swift* uses a grazing incidence Wolter I telescope to focus X-rays on a CCD (Burrows et al. 2005). The instrument has an effective area of 110 cm^2, 23.6 arcmin field of view (FOV), 15 arcsec resolution (half-power diameter), and it covers an energy range of 0.2–10 keV. The windowed timing (WT) mode data were used to obtain the spectrum from *Swift*-XRT. Source photons were extracted using a box region with a length of 40 pixels and width of about 20 pixels. Events with grades 0–2 were selected. The spectral data were rebinned by GRPPHA 3.0.0 with a minimum of 20 photons per bin. Standard auxiliary response files and response matrices were used.

A combined spectral fit was obtained for PCA and XRT data by normalizing the PCA spectrum with the XRT spectrum. The PCA and XRT spectra in the energy range of 0.3–30 keV were fitted by using XSPEC with a cutoff power law with line-of-sight absorption. The line-of-sight absorption was fixed to a neutral hydrogen column density of 1.56×10^{20} cm^{-2} (Kalberla et al. 2005).

Swift-XRT light curves are obtained from *Fermi* multi-wavelength support program Web sites[8] and are used in this study.

The "Dwell" data from *RXTE*-ASM were obtained from the ASM Web site[9] and were analyzed with the method discussed in Chitnis et al. (2009). A daily average flux between 15–50 keV from *Swift*-BAT was obtained from the BAT Web site,[10] a detailed analysis procedure can be found in Krimm et al. (2013).

The *Swift*-UVOT (Roming et al. 2005) data were used to obtain fluxes in UVW1, UVM2, and UVW2 filters for different epochs. The snapshots of every individual observation were integrated with the *uvotimsum* task and then were analyzed with the *uvotsource* task. A source region with a 10″ radius was selected around the source, while the background was extracted from a circular region of 1′, which is centered in a source-free region. The flux obtained was corrected for a Galactic extinction of $E_{(B-V)} = 0.019$ mag as given by Schlegel et al. (1998) in each spectral band.

2.3. Fermi-LAT

The *Fermi*-LAT is a pair production telescope (Atwood et al. 2009) on board the *Fermi* spacecraft. LAT covers the energy range from 20 MeV to 300 GeV with an FOV of $\geqslant$2.5 sr. The *Fermi*-LAT γ-ray data of Mrk 501 over the period of 450 days (MJD: 55560- 56010) were obtained from the Web site.[11] Data above 200 MeV were analyzed using the standard analysis procedure *(ScienceTools-v9r31p1)* provided by the *Fermi*-LAT collaboration.

A circular region with a 10° radius, the "region of interest (ROI)," was chosen around Mrk 501 for event reconstruction from the so-called "diffuse" event class data that has the maximum probability of being the source photons. Events

[6] http://james.as.arizona.edu/p˜smith/Fermi/
[7] http://www.astro.caltech.edu/ovroblazars/
[8] http://www.swift.psu.edu/monitoring/
[9] http://xte.mit.edu/
[10] http://swift.gsfc.nasa.gov/results/transients/
[11] http://fermi.gsfc.nasa.gov/

Table 1
HAGAR Observations of Mrk 501 in 2010 and 2011

Epoch	Total Duration (min) (Pairs)	Excess Number of ON source events	Mean γ-Ray Rate (/min)	Significance σ
2010 Mar 22–2010 May 20	400.2 (10)	1577.0 ± 511.9	3.9 ± 1.3	3.1
2011 Mar 31–2011 Apr 10	279.5 (7)	989.2 ± 399.6	3.5 ± 1.4	2.5
2011 Apr 28–2011 May 10	348.6 (9)	2308.1 ± 454.9	6.6 ± 1.3	5.1
2011 May 26–2011 Jun 03	212.6 (6)	967.1 ± 369.2	4.6 ± 1.7	2.6

having a zenith angle $< 100^\circ$ are only retained to avoid the background from Earth's albedo. The spectral analysis of the resulting data set was carried out by including a galactic diffuse emission component model (gal_2yearp7v6_v0.fits) and an isotropic background component model (iso_p7v6source.txt) with a post-launch instrumental response function P7SOURCE_V6, using unbinned maximum likelihood analysis (Cash 1979; Mattox et al. 1996). A power law was used to model the source energy spectrum above 200 MeV, with an integral flux and photon index as free parameters. The flux and spectrum were determined by using an unbinned GTLIKE algorithm.

2.4. HAGAR

The HAGAR telescope array is an Atmospheric Cherenkov Telescope array used for detecting VHE γ-rays from the celestial sources. This array uses the wavefront sampling technique and is located at the Indian Astronomical Observatory (IAO), Hanle (32° $46'$ $46''$ N, 78° $58'$ $35''$ E), in the Ladakh region of India, at an altitude of 4270 m. HAGAR consists of an array of seven telescopes arranged in the form of a hexagon, with one telescope at the center. Each telescope is separated by a 50 m distance from its neighboring telescope. These telescopes use an alt-azimuth mounting system (Gothe et al. 2013). All seven telescopes have seven para-axially mounted front-coated parabolic mirrors with a diameter of 0.9 m each, with a UV-sensitive photo-tube at the focus of each individual mirror. These parabolic mirrors have an f/D ratio of one, and they were fabricated by using 10 mm thick float glass sheets. The FOV of HAGAR telescope is 3° FWHM. The photomultiplier tubes (PMT), which are mounted at the focus of these mirrors, are manufactured by Photonis (XP2268B) and have a peak quantum efficiency of 24% at 400 nm. The high voltages fed to these PMT are monitored and controlled by C.A.E.N controller module (SY1527). In addition to recording signals from individual PMTs, the signals from the 7 PMTs of a telescope are linearly added to form a telescope pulse that is also recorded. The presence of any four telescope pulses above a preset threshold value and within a window of about 150 ns forms the trigger for initiating data acquisition. The typical trigger rate was about 12 Hz.

The CAMAC-based Data Acquisition (DAQ) system is used in HAGAR. Relative arrival time of the Cherenkov shower front at each mirror is recorded for each event, as measured by time-to-digital converters with a resolution of 250 ps. The Cherenkov photon density at each telescope is measured by the total charge present in PMT pulses using 12 bit charge-to-digital converters and a real-time clock (RTC) module synchronized with GPS is used to record the absolute arrival time of these events accurate up to μs. In addition to this, a parallel DAQ using commercial waveform digitizers with a sampling rate of 1 GS/s (ACQIRIS make, model DC271A) is also used to record telescope pulses.

The energy threshold of the HAGAR telescope array is estimated to be 208 GeV for vertically incident γ-ray showers for a $\geqslant$ four-fold trigger condition, for which the corresponding collection area is 3.44×10^8 cm^2. The corresponding sensitivity is such that HAGAR will detect a Crab-nebula-like source at a significance level of 5σ in 17 hr of observation (Saha et al. 2013), with no additional criteria for the rejection of background cosmic-ray events.

Observations of Mrk 501 were made during 2010 March–May and 2011 March–June on Moon-less, clear nights using the HAGAR telescope. Observation details are provided in Table 1. The observations were carried out by tracking the source or background region with all seven telescopes. Each source (ON run) was followed (or preceded) by a background (OFF run) with the same exposure time (typically 40 minutes) covering the same zenith angle range as that of the source to ensure that observations were carried out at almost the same energy threshold. Selection criteria were applied to identify good quality data. Data were analyzed according to the procedure discussed in Shukla et al. (2012). In this procedure, the Cherenkov shower front is approximated with plane front and space angle, i.e., the angle between shower axis and pointing direction of telescope is estimated. The γ-ray signal is estimated by comparing the space angle distribution from an ON–OFF pair. Only events with signals in at least five telescopes ($\geqslant$five-fold) were analyzed to reduce systematic errors, which corresponds to an energy threshold of 250 GeV for γ-rays.

2.5. ARGO-YBJ

The ARGO-YBJ experiment situated at the Yangbajing Laboratory, Tibet at 4300 m a.s.l. was designed to study cosmic γ-radiation, at an energy threshold of $\sim$100 GeV, by means of the detection of small-size air showers. ARGO-YBJ consists of a single layer of Resistive Plate Counter (RPC) detectors covering an area of $\sim$6700 m^2 to detect air showers. We have used published TeV γ-ray data of Mrk 501 from ARGO-YBJ, collected during 2011 October 17 to November 22 (Bartoli et al. 2012).

3. RESULTS

Mrk 501 was observed during 2010 and 2011 using the HAGAR telescope when it was in a moderate state of activity, and VHE γ-rays were detected from it. The source was detected with a 5σ significance during 2011 May (MJD: 55679–55692) when the average flux reached a peak flux of $\sim$1.5 Crab units (1 Crab unit = 4.2 counts/minute for at least five telescopes triggering). The average integral flux in this observation period above 250 GeV is found to be 4.04×10^{-10} ph^{-1} cm^{-2} s^{-1}. The light curve based on HAGAR observations during 2011 March–June is shown in Figure 1. The TeV γ-rays from Mrk 501 are detected at a total significance of 6.7σ over the observation period of two years. The source had brightened up moderately during 2011 over the entire electromagnetic spectrum. The multi-wavelength light curves from radio to γ-rays are used to

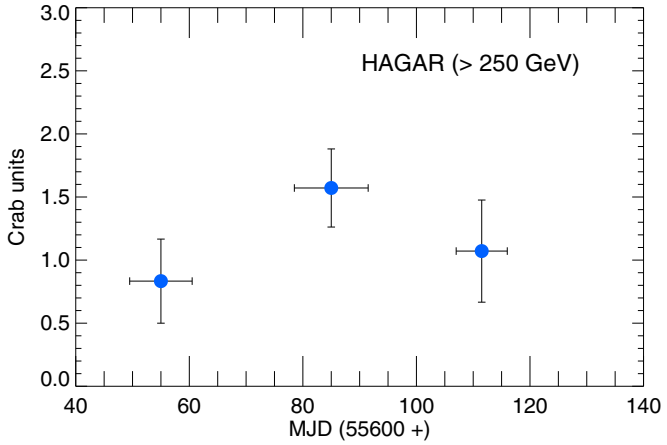

Figure 1. HAGAR light curve of Mrk 501 during 2011.

Table 2
Time Periods Used to Obtain SEDs

Epoch	MJD	Dates	Days
S1	55651–55661	2011 Mar 31–2011 Apr 10	10
S2	55679–55692	2011 Apr 28–2011 May 11	13
S3	55707–55716	2011 May 26–2011 Jun 3	9
S4	55860–55890	2011 Oct 26–2011 Nov 25	30
S5	55919–55934	2011 Dec 24–2012 Jan 08	15

understand its flux levels and variability. The multi-waveband quasi-simultaneous light curve of Mrk 501 during 2011–2012 is plotted in Figure 2. A few moderate and high states are identified during this period to study the spectral variation with the activity in X-ray and γ-ray bands. SEDs were obtained for five such states by fitting multi-wavelength data with the SSC model. Details of these states are provided in Table 2.

3.1. Flux and Spectral Variation During 2011–2012

Multi-wavelength flux and spectral variability of Mrk 501 as measured and reported by several ground- and space-based instruments during 2011–2012 are presented in this section. The multi-waveband quasi-simultaneous light curve of Mrk 501 during 2010 December 30 to 2012 March 24 is shown in Figure 2. The panels, in descending order, correspond to data from OVRO (15GHz), SPOL (optical *V* band), *Swift*-XRT (2–10 keV), *Swift*-BAT (15–50 keV), *Fermi*-LAT (0.2–2 GeV), and *Fermi*-LAT (2–300 GeV). The bottom panel corresponds to HAGAR data above 250 GeV.

Mrk 501 was found to be variable in all the wavebands during the time span of 2011 January to 2012 March with a few active states during this period. A clear variation of flux over a period of one year is observed in the radio, optical, X-rays, and γ-rays. We found that the source was brightest in X-rays and γ-rays at the end of the year when it showed a couple of flares in X-rays and γ-rays. During this period of active states, a few X-ray flares were observed by *Swift*-BAT (15–50 keV). Source showed flaring behavior during 2011 October 26–2011 November 25, and the peak flux in this duration was observed on MJD:55873; however, the peak flux observed by *Swift*-XRT was on MJD: 55931.09. The X-ray (*Swift*-BAT) light curve shows mild correlation with a high-energy γ-ray light curve (2–300 GeV). This correlation appears to be stronger in the high state of the source. A similar trend was also reported earlier by Gliozzi et al. (2006). Fluxes in different wavebands during HAGAR observation periods are also plotted; see Figure 3. The source was bright during 2011 May in the entire electromagnetic spectrum.

Table 3
Fermi-LAT Spectrum

Epoch	Flux (0.2–300 GeV) $\times 10^{-8}$ ph^{-1} cm^{-2} s^{-1}	Photon Index 0.2-300 Ge V	TS	XRT-PCA Index
S1	3.8 ± 0.3	1.59 ± 0.14	102	1.95
S2	5.12 ± 0.88	1.66 ± 0.13	126	1.87
S3	1.78 ± 0.34	1.27 ± 0.21	67	2.11
S4	4.5 ± 0.23	1.62 ± 0.09	297	1.75
S5	5.9 ± 0.45	1.46 ± 0.10	276	1.59

The *Fermi*-LAT light curves at different energies (0.2–300 GeV, 0.2–2 GeV, and 2–300 GeV) during the period from 2010 December 30 to 2012 March 24 are plotted with a bin size of 15 days in Figure 4. The top two panels of this figure correspond to a flux and photon index of a low γ-ray energy band (0.2–2 GeV), next two panels correspond to flux and photon index of high γ-ray energy band (2–300 GeV). The two bottom panels of this figure correspond to the flux and photon index of a full γ-ray energy band (0.2–300 GeV). Photon indices are only plotted for those bins that have more than 5σ detection. The LAT observed flux and spectral variation in the low-energy γ-ray band (0.2–2 GeV) is found to be different compared to the high-energy band (2–300 GeV).

Studies of spectral properties of Mrk 501 in X-ray and γ-ray bands show significant spectral variability during 2011 in both the bands. Comparison of spectral variation with the activity of the source was carried out for the period (MJD: 55651-55934) using *RXTE*-PCA, *Swift*-XRT, and *Fermi*-LAT instruments. X-ray and γ-ray spectral indices were obtained for several flux states and given in Table 3. This table contains time interval, γ-ray flux above 0.2 GeV, γ-ray photon index, and values of likelihood test statistics (TS) as obtained from the *Fermi*-LAT analysis for which spectra are made, and the last column contains X-ray indices as obtained from the combined fit of *Swift*-XRT and RXTE-PCA data.

The *Fermi*-LAT collaboration had reported the value of the photon index to be 1.78 based on the first 480 days of their observations of Mrk 501. This refers to an average spectrum mostly during the quiescent state. They detected remarkable spectral variability where the observed spectral index ranges from hardest value of 1.52 ± 0.14 to the softest 2.51 ± 0.20 (Abdo et al. 2011). This change in the spectrum was not found to be correlated with the measured flux variations above 0.3 GeV. We also have detected large spectral variability during 2011 in our study. We found much harder spectra than Abdo et al. (2011) during our study; the hardest spectrum was detected during S3 with a value of 1.27 ± 0.21 in the energy band of 0.2–300 GeV (for details, see Table 3). Using 15 day bins, we have also detected very hard spectra of indices $\sim$1.2 during our 2011–2012 analysis, at higher-energy γ-rays band (see the fourth panel of Figure 4). The spectral variability is also seen in the X-ray band during 2011.

The cross plot between the γ-ray flux and photon index, shown in Figure 5, clearly shows two populations, one for low-energy bins of 0.2–2 GeV and the second for bins of 2–300 GeV. The photon index increases with the increase in flux for lower energies (plotted in the green square), but the

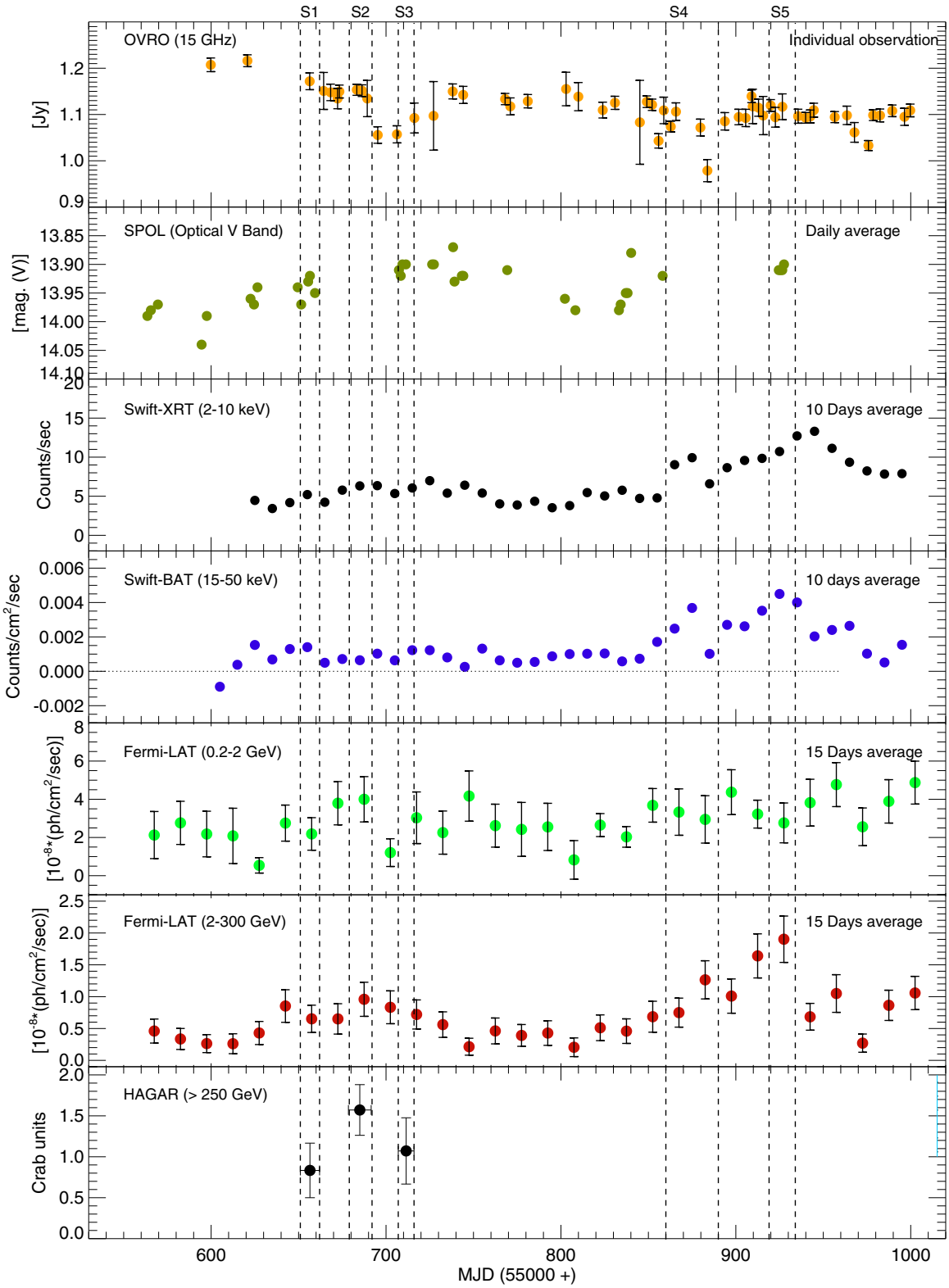

Figure 2. Multi-wavelength light curves of Mrk 501 during 2011–2012. The bin size (in days) used for averaging the flux at different energy bands is mentioned at the right corner. The bin size for HAGAR observations is marked using x-error bars. The vertical dashed lines represent the periods of moderate and high flux states for which SEDs are obtained; details of these states are provided in Table 2.

cross plot shows scatter in case of high-energy γ-rays, and no significant trend is visible (plotted in red downward triangles). This property indicates that low-energy γ-rays may be produced in a different emission zone having a slightly different electron energy distribution and magnetic field than higher-energy VHE γ-rays in Mrk 501.

In addition to the results discussed in this paper, the recent *Fermi*-LAT observations of Mrk 501 challenge our present

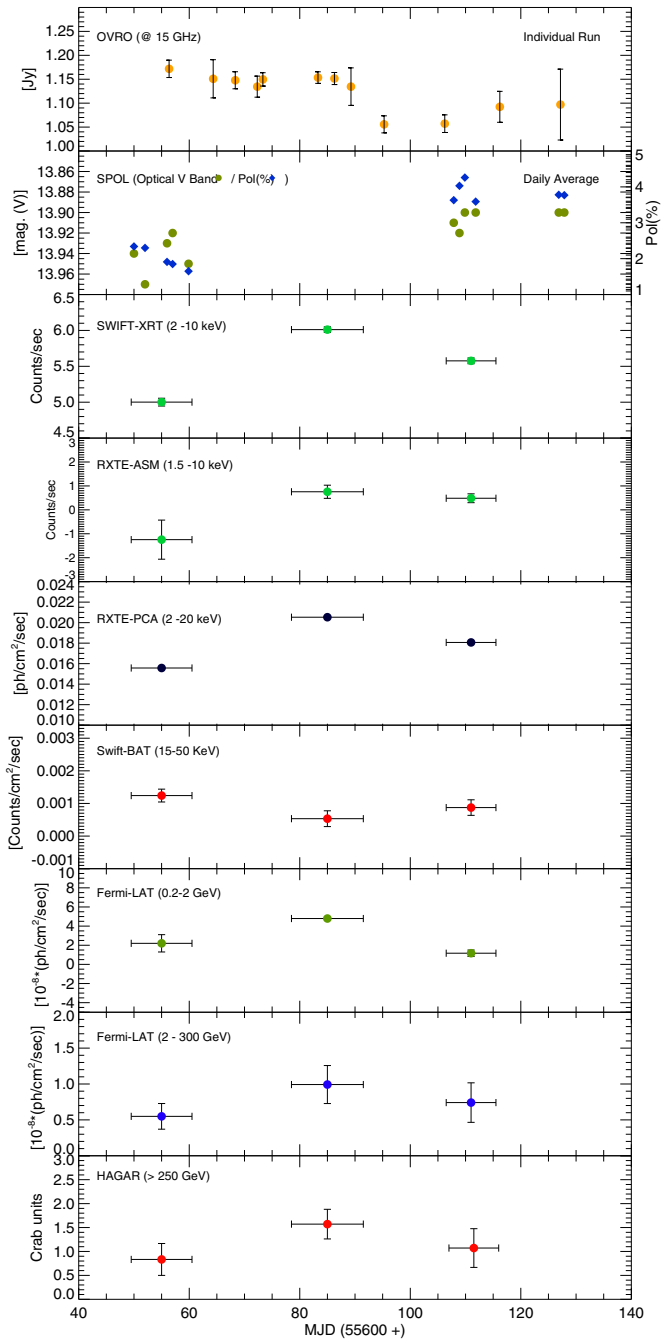

Figure 3. Multi-wavelength light curve of Mrk 501 during HAGAR observations.

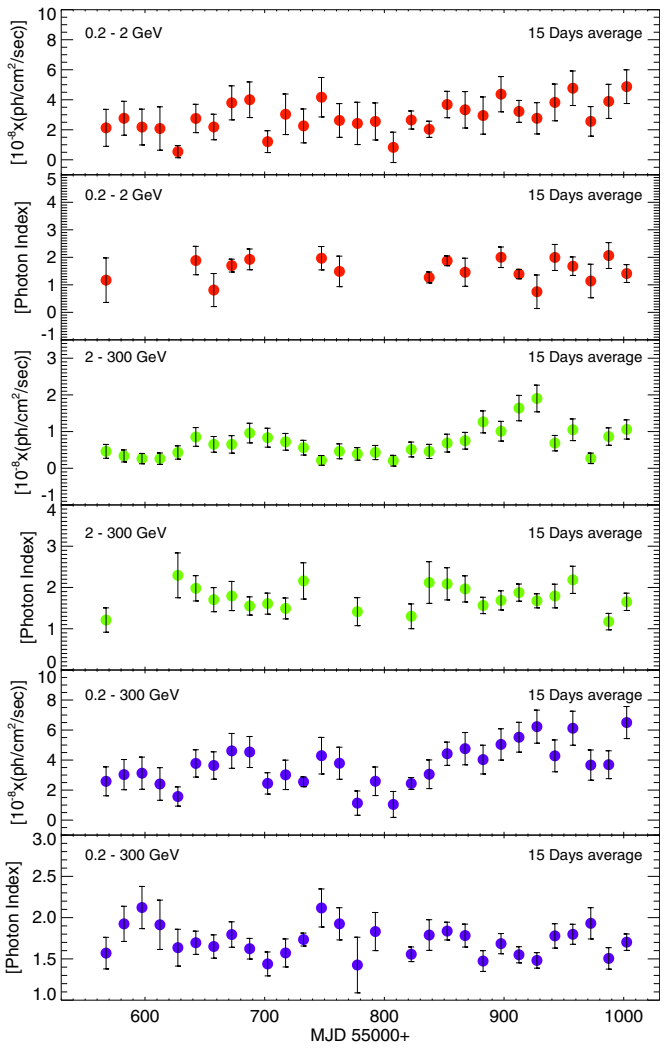

Figure 4. High-energy γ-ray light curve of Mrk 501 and photon index from *Fermi*-LAT during 2011–2012.

understanding about this source (Neronov et al. 2012). New evidence for the presence of very hard intrinsic γ-ray spectra obtained from *Fermi*-LAT observations has challenged the theories of the origin of VHE γ-rays. Several very interesting and viable explanations for the observed hard spectra have been proposed in recent years. A hard γ-ray spectrum could be obtained much more easily in the hadronic scenario as discussed in the proton synchrotron model (Aharonian 2000), whereas achieving a hard spectrum from leptonic models is more demanding. Some viable scenarios, such as relativistic Maxwellian-type electron energy distributions that are formed by a stochastic acceleration process as a cause of hard spectra (Lefa et al. 2011b) or the hard spectra produced by an electromagnetic cascade initiated by very high energy γ-rays in the intergalactic medium (Neronov et al. 2012) are available in the literature.

4. SPECTRAL ENERGY DISTRIBUTION

Since its detection at VHE γ-rays, the broadband emission from Mrk 501 has been explained mostly using one-zone models in literature, which was quite effective to explain the observed data from radio to γ-rays (Sambruna et al. 2000; Krawczynski et al. 2000). The main reason of the apparent success of the one-zone model was the lack of the simultaneous multi-waveband data and the absence of data at low γ-ray energies. The broadband spectral and flux variability studies enabled by the multi-wavelength campaigns carried out during the recent years revealed the rather complex behavior of Mrk 501. The modeling of the Mrk 501 SED assuming a homogeneous single emission zone is a very simplified situation. The broadband emission from the blazar may be produced in an inhomogeneous region. The observed emission from Mrk 501 could be due to a complex superposition of multiple emission zones. The study carried out by Neronov et al. (2012) and the one presented here indicate the existence of two separate components in the spectrum: one for low-energy γ-rays and the other for

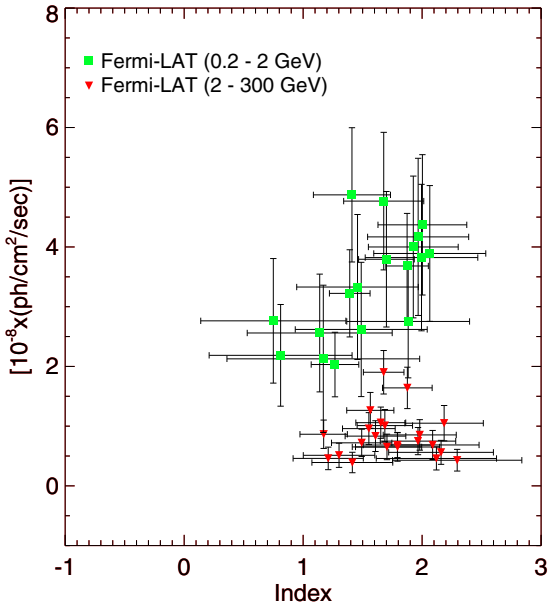

Figure 5. Cross plot: Flux vs. photon index during 2011 with 15 day bins

high-energy γ-rays. For example, emission from a single zone is not enough to explain tlhe broadband emission of Mrk 501 as shown in Figure 6, where Mrk 501 SED is modeled using a single zone.

We have considered a two-zone scenario to explain the broadband SED of Mrk 501. We assume that the observed broadband SED is a sum of two components (two zones) that are radiating simultaneously and boosted with almost the same Doppler factor. These two zones have comoving radii $R_{\rm in}$ and $R_{\rm out}$ and travel with a bulk Lorentz factor Γ toward the observer. The emission zones are filled with randomly oriented uniform magnetic fields $B_{\rm in}$ and $B_{\rm out}$ and isotropic population of non-thermal electrons. The energy spectra of the injected electrons in the jet frame are described by broken power laws with low-energy ($E_{\rm min}$ to E_b) and high-energy (E_b to $E_{\rm max}$) components with indices of p1 and p2. The outer zone is responsible for the quiescent state flux, and the other compact inner zone, which is close to the black hole, is responsible for flaring activity in the jet. The broadband emission from the blazar zone is sum of the flux of the quiescent component and active component.

The radius of the emission zone is constrained by the variability timescales. The comoving radius of the emission zone is defined as

$$R \sim c\delta t_{\rm var}/(1+z). \quad (1)$$

The values of $t_{\rm var}$ for both zones are provided in Table 4. These values are consistent with the flux variability observed in Mrk 501 during our study period and are available in literature (Acciari et al. 2011 and references therein).

Five different flux states have been identified during 2011, when the source was in a moderate and high state of activity (see Figure 2 and Table 2). An average TeV spectrum as observed by ARGO-YBJ during October 17 to November 22 is used to model S4 state. The SED obtained as a result of the 4.5 month-long multi-frequency campaign (2009 March 15–2009 August 1) organized by *Fermi* and the MAGIC collaboration (hereafter MAGIC SED; Abdo et al. 2011) is also modeled with a two-zone model for comparison. Multi-waveband data for all six SEDs (S1 to S5 and MAGIC SED) are fitted with a two-zone SSC model, and satisfactory fits are obtained (see Figures 7–12). One more point to be noted is that the BAT flux covering the energy range of 15–50 keV during the S1 state is somewhat higher than the fitted model, whereas the fitted model agrees well with the data from *Swift*-XRT and *RXTE*-PCA together covering the energy range of 0.3–30 keV. For other states, the BAT flux seems to

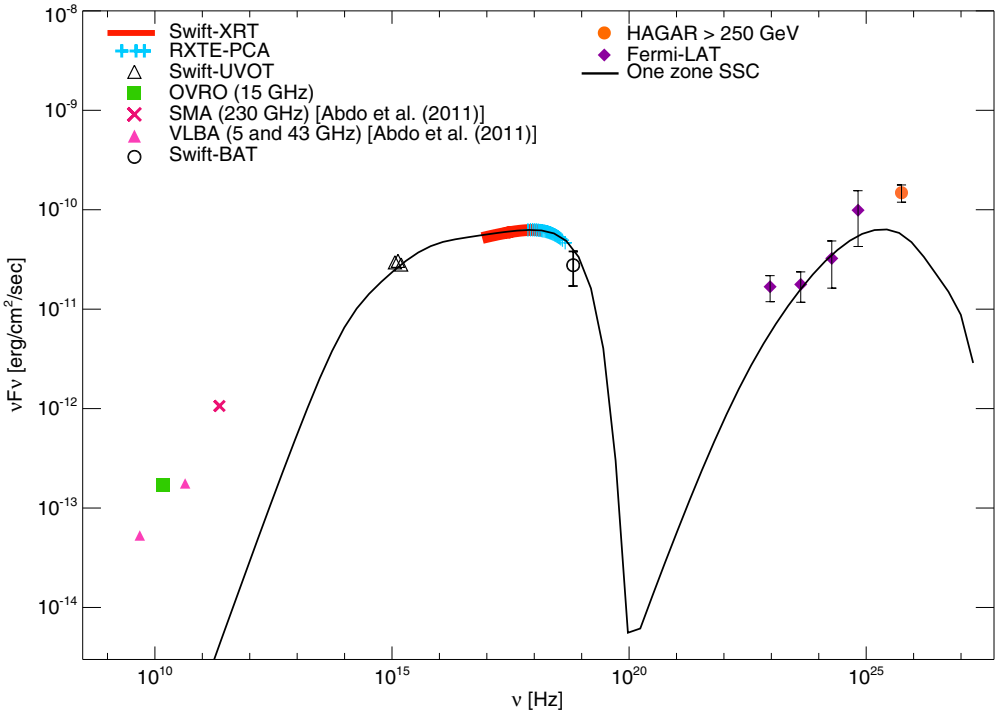

Figure 6. One-zone SED of Mrk 501 during 2011 April–May [S2]

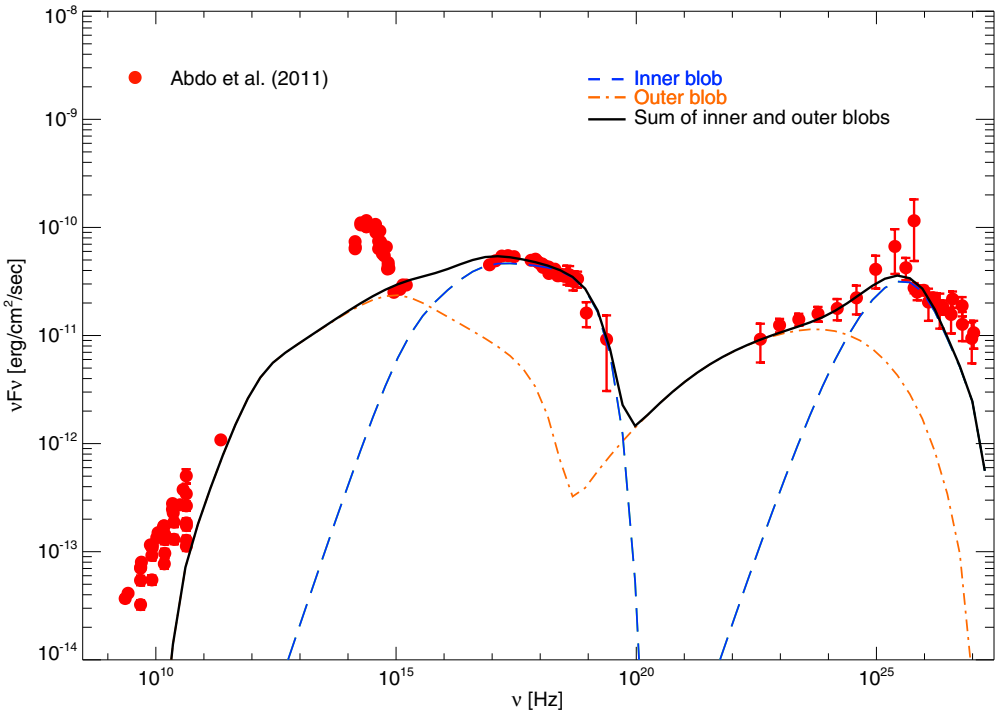

Figure 7. Two-zone spectral energy distribution of Mrk 501, as observed and presented in MAGIC SED. The solid black line shows the best-fit two-zone model to the data, with the best-fit parameters listed in Table 4.

Table 4
SED Parameters

State	T_var (hr)	Magnetic Field (G)	Doppler Factor (δ)	[a] log $E_{\rm min}$ [eV]	[b] log $E_{\rm max}$ [eV]	[c] log $E_{\rm break}$ [eV]	p1	p2	[d] U_e [10^{-3}] (erg/cc)	[e] η [u_e'/u_B']
MAGIC (Outer)	48	0.032	12.07	8.6	11.6	10.10	2.4	3.50	1.8	44.2
S1 (Outer)	48	0.028	12.07	8.9	11.6	10.10	2.4	3.95	1.0	32.0
S2 (Outer)	48	0.028	12.07	8.9	11.6	10.10	2.4	3.95	1.6	51.3
S3 (Outer)	48	0.028	12.07	8.9	11.6	10.10	2.4	3.95	1.0	32.0
S4 (Outer)	48	0.028	12.07	8.9	11.6	10.10	2.4	3.95	1.25	40.1
S5 (Outer)	48	0.028	12.07	8.9	11.6	10.10	2.4	3.95	1.0	32.0
MAGIC (inner)	6.9	0.08	12.07	10.0	11.95	10.80	2.0	3.05	11	43.2
S1 (inner)	6.9	0.075	12.07	9.75	11.85	10.55	2.0	2.9	18	80.4
S2 (inner)	6.9	0.056	12.07	10.2	11.95	10.45	2.0	2.85	27	216.0
S3 (inner)	6.9	0.075	12.07	10.2	12.00	10.45	2.0	3.1	20	89.4
S4 (inner)	6.9	0.056	12.07	9.7	12.05	10.90	2.0	2.5	30	240.0
S5 (inner)	6.9	0.075	12.07	8.7	11.90	11.35	2.0	2.6	32	143.0

Notes.
[a] $E_{\rm min}$: minimum value of energy of the electrons present in the emission zone.
[b] $E_{\rm max}$: maximum value of energy of the electron present in the emission zone.
[c] $E_{\rm break}$: break in the electron injection spectrum.
[d] U_e: electron energy density.
[e] η: equipartition coefficient.

roughly agree with the fitted model and measurements from lower-energy X-rays.

No change is observed in the jet flow (Doppler factor) during 2011 in fitted SED. Magnetic field strength in the outer zone shows no variation among these states, but SED modeling of the inner zone indicates that the magnetic field in this zone varies with state. We found comparatively lower magnetic field strength during active states S2 and S4 in the inner zone, but we found higher magnetic field in high state S5 by SED modeling. We have also not seen any significant change in the electron energy distribution of the outer zone but change is indicated in the inner zone. Higher electron energy density is found at the time of activity in the inner zone. Also, we noticed a significant change in the electron energy spectral index after the break (p2) in this zone.

5. DISCUSSION

Mrk 501 is a core-dominated radio source, with a one-sided jet on a parsec scale, which extends until ∼500 pc. This jet

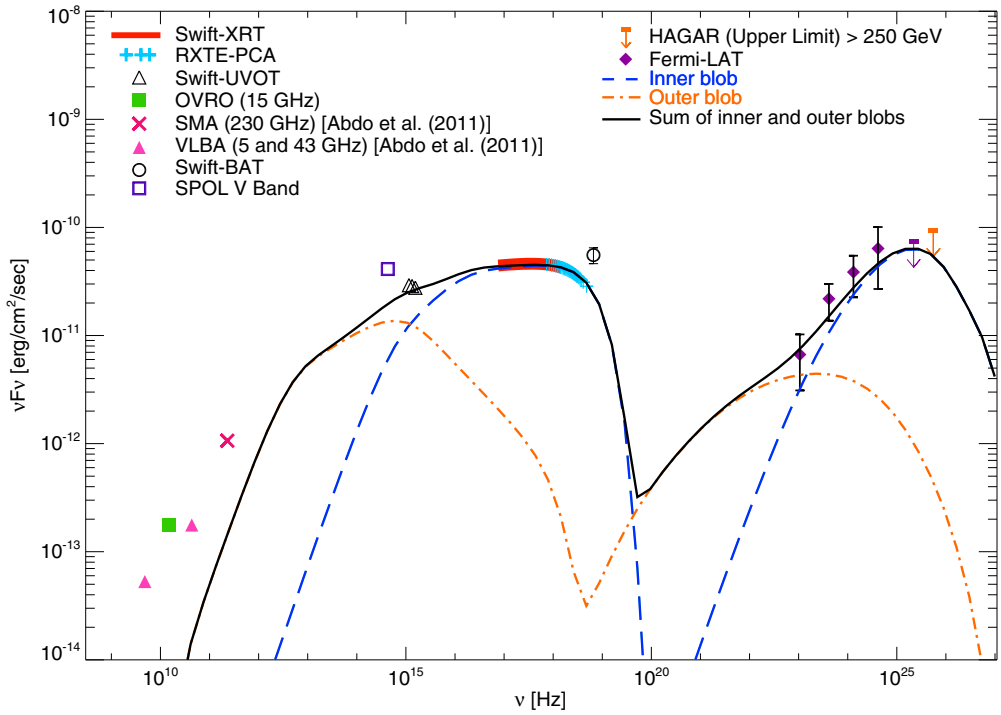

Figure 8. Two-zone SED of Mrk 501 during 2011 March–April [S1].

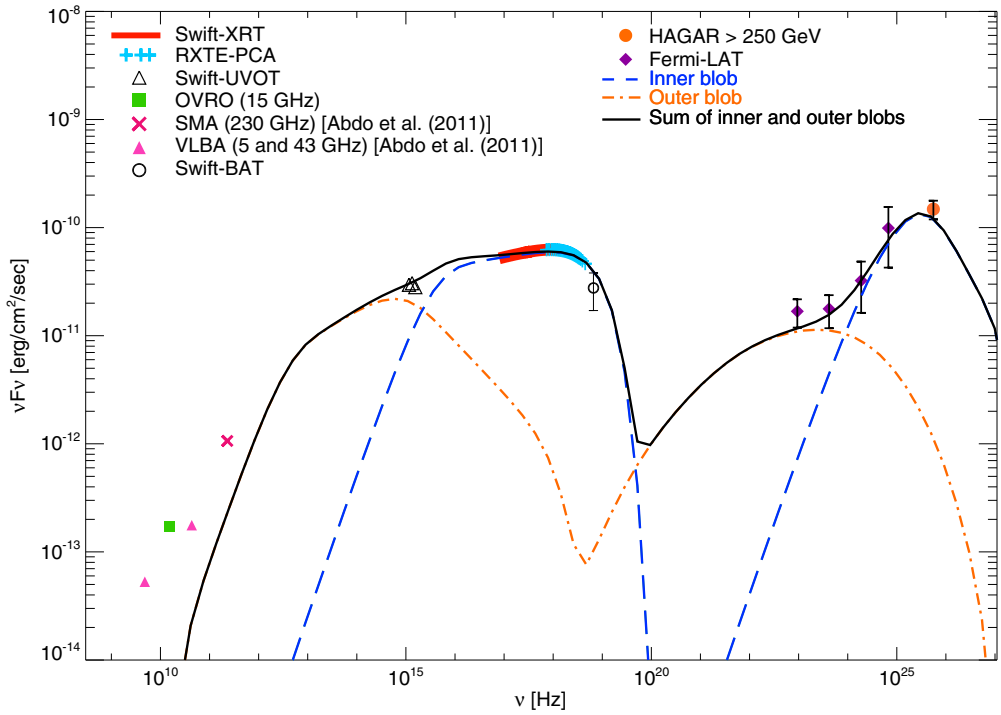

Figure 9. Two-zone SED of Mrk 501 during 2011 April–May [S2].

shows several sharp bends followed by rapid expansion and limb brightening structures on physical scale of ∼1 pc as seen by Giroletti et al. (2004).

In recent years, several attempts were made to model the SED of Mrk 501 with multi-zone scenarios (Ghisellini et al. 2005; Graff et al. 2008; Giannios et al. 2009; Lefa et al. 2011a) or adding extra breaks in the injected electron distribution (Abdo et al. 2011). Alternatively, the SED could also originate from a two-component spine-sheath structure of the jet transverse to its direction (Ghisellini et al. 2005), as suggested by the complex very long baseline interferometry (VLBI) radio jet morphology of Mrk 501 Giroletti et al. (2004). However, the energy transport in blazar jets generally occurs along the jet axis as witnessed by the motion of VLBI radio knots that logically

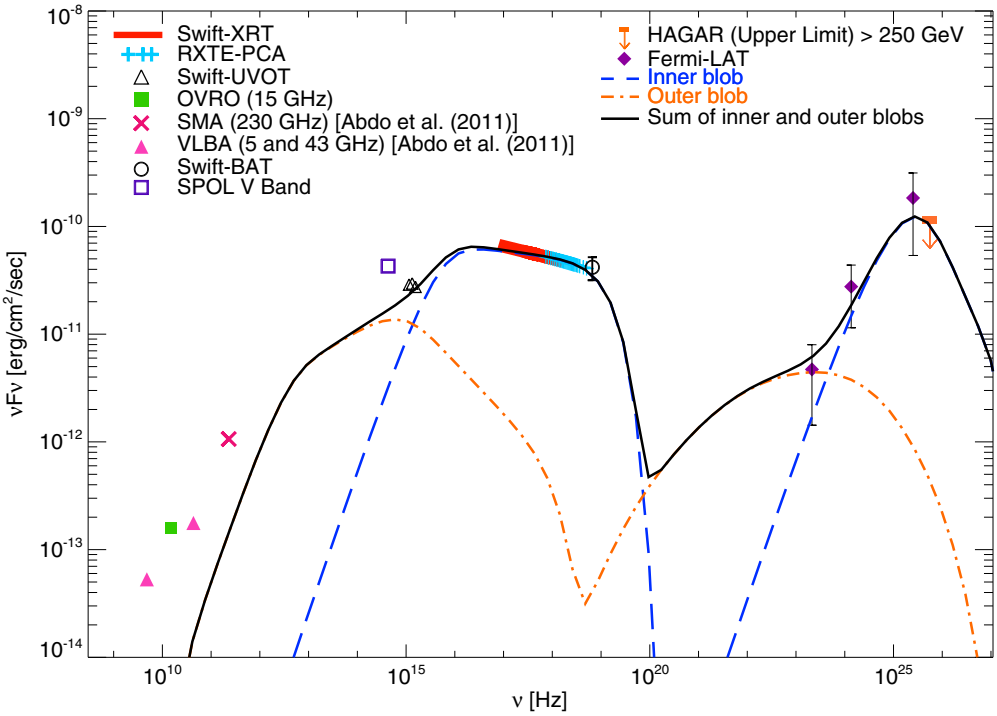

Figure 10. Two-zone SED of Mrk 501 during 2011 June [S3].

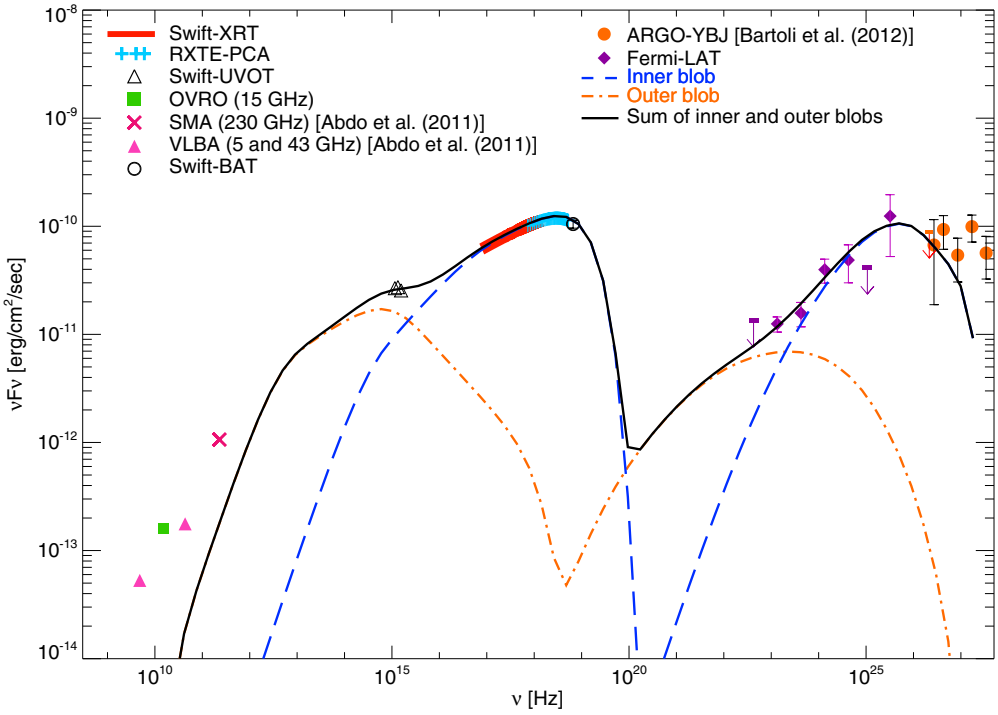

Figure 11. Two-zone SED of Mrk 501 during 2011 November [S4].

suggest connecting the flux variability with the longitudinal evolution of the components.

In this section, we discuss the implications of the physical parameters of the source resulting from the SSC modeling of the SED. We also try to understand properties of the electron energy distribution emerging from SED modeling and constrain the physical processes responsible for the particle acceleration. We also examine the broadband variability of Mrk 501 in the framework of our two-zone model.

5.1. Variability

An alternative way to constrain the physical parameters of the jet is to model its flux variability. Measurement of fast and rapid

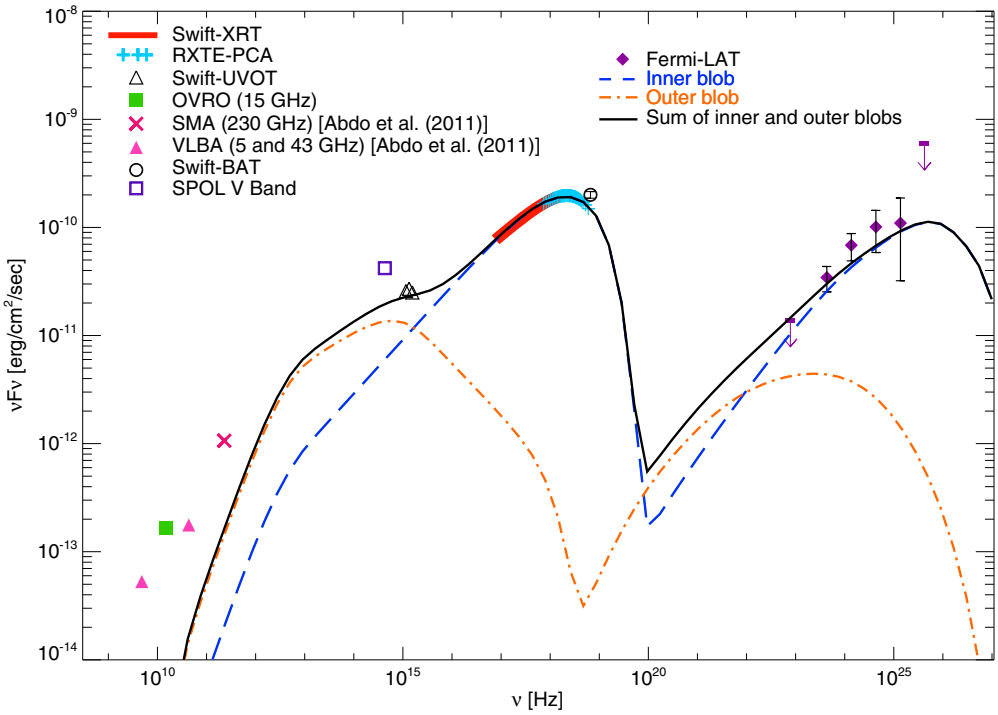

Figure 12. Two-zone SED of Mrk 501 during 2011 December [S5].

flux variability can shed light on motions of the bulk outflows of the plasma in the innermost region of jets that is well beyond the current imaging capabilities of telescopes in any part of the electromagnetic spectrum.

In the SSC scenario, the highest-energy tail of the electron energy distribution ($\gamma \geqslant \gamma_{br}$) is responsible for the production of the observed X-ray synchrotron continuum at $\geqslant$0.5 keV in HBLs, while the TeV γ-rays might be produced through upscattering of synchrotron photons by the same population of electrons. The observed optical and X-ray variability during 2011–2012 may be explained by the injection of fresh electrons in emission zones and cooling of the electrons due to the SSC mechanism. Mrk 501 also shows energy-dependent flux and spectral variability in γ-rays. The source flux varies from lower energies (0.2–2 GeV) to higher energies (2–300 GeV). The observed γ-ray variability is mainly divided into two bands, $<$2 GeV and above 2 GeV. The 0.2–2 GeV γ-rays observed by *Fermi*-LAT could be produced by low-energy electrons through IC scattering of UV synchrotron photons. The observed HE ($>$2 GeV) γ-rays by *Fermi*-LAT and VHE γ-rays by HAGAR could be produced by IC scattering of the electrons having a Lorentz factor in the range $\sim 10^4$–10^5.

Mrk 501 was detected in a moderate activity state during 2011 May by HAGAR, as seen in the last panels of Figures 2 and 3. A positive correlation between low-energy X-rays and γ-rays is seen during this period, with the peak flux being observed in 2011 May in the γ-ray and X-ray wavebands. Observed flux enhancement during the S2 period can be explained by the injection of fresh electrons in the active zone (inner zone) of the jet. These electrons may be accelerated to higher energies by shock in the jet. Two-zone spectral modeling of this period suggests that the injected electron spectrum in the inner zone has a power-law of index 2, which could arise due to Fermi first-order mechanism. Moreover, the *Swift*-BAT light curve is found to be anti-correlated with the other wavebands, and we cannot conclusively say why the flux in the *Swift*-BAT band is found to be high during S1.

5.2. Application of the Two-zone Model in Mrk 501 Multi-waveband Data During 2011

The multi-frequency data set provides an opportunity to obtain broadband SED of Mrk 501 in the quiescent and moderate states, and it also allows comparison between these flux states. In the work presented here, we have compared five different flux states of Mrk 501 during 2011, along with the quiescent state SED observed by Abdo et al. (2011). We have modified the single-zone model developed by Krawczynski et al. (2004) to a multi-zone model and used it to explain broadband emission from Mrk 501. Details of this one-zone model can be found in Krawczynski et al. (2004). The same model was also used by Shukla et al. (2012) to explain the SED of Mrk 421. The best-fit parameters of the fitted two-zone model to the data are listed in Table 4.

We have found that γ-ray-emitting zones are very close to the black hole around $\sim$0.08 pc, which is consistent with other results presented in the literature. The inferred magnetic field from the modeling of the SED by our model is also in good agreement with the magnetic field claimed for the partially resolved radio core of Mrk 501 (Giroletti et al. 2004). But in our model, the source is not found in equipartition with the relativistic electrons along with magnetic field. On the other hand, the source is consistent with being in equipartition with the relativistic electrons in the spine-sheath model given by Ghisellini et al. (2005). From our study of multi-waveband SED modeling, we also infer that plasma in the jet is moving with a Doppler factor of $\sim$12, and it does not change with the flux state and time. This value is consistent with other previous works (Abdo et al. 2011). Also, we have not detected any change in the speed of the jet in the γ-ray-emitting

zone (<0.1 pc). The electrons in these blobs are accelerated through the Fermi first-order mechanism producing a power-law distribution. We have found the inner blob has a much narrower electron distribution than the outer blob, with a high minimum cutoff for $\gamma_{\rm min}$. This blob is responsible for activity in the blazar zone and also the observed hard spectrum in the source. A narrow electron distribution can produce a very hard spectrum; similar suggestions were also made by Tavecchio et al. (2009), Katarzyński et al. (2006), and Lefa et al. (2011b). The electron population of the outer zone is evolved and old, and this population has suffered radiative and adiabatic losses. We have observed via SED fitting that the contribution of the outer zone is not constant and it varies with flux state. Among the six flux states we discussed in this work, we found the outer zone contributes significantly to the γ-ray hump in all the states except S5. This could be possible only if the outer zone during S5 is not left with high-energy electrons at the time of activity. We found that at the time of activity, the inner blob becomes dominant and it may produce a hard spectrum at the highest energies. The observed SED of Mrk 501 is the sum of total radiation emitted by two zones and the shape of SED depends on the relative contributions from each zone. If both the zones contribute to the total observed flux, then SED might be observed with a plateau at lower-energy γ-rays and a hard spectrum at the highest energy. The difference between the spectral indices below and above the break energy $\Delta p = p_2$-p_1 determined by SED modeling are close to 1 in the case of S1, S2, S3, and MAGIC SED for the inner zone (see Table 4). The value Δp = 1 is expected as a result of the classical synchrotron cooling break for a uniform emission region.

The observed LAT spectrum during 2011 May when the source was in a moderate bright state shows a plateau in the SED at lower energies ~(0.2–5 GeV) and a break in the slope at ~5 GeV (see Figure 9). A hard spectrum with a photon index of 1.5 is detected in higher-energy (2–300 GeV) bands during these observations. A similar behavior was also reported during a flare observed in the first 480 days of the *Fermi*-LAT operation (2008–2009) in Abdo et al. (2011). The spectrum of this flare was found to be very hard/flat (~1.1) in the 10–200 GeV range. The SED in the 0.3–200 GeV range during this flare also shows a break in the slope, around 10 GeV (Neronov et al. 2012). Very hard spectra (<1.3) are detected in the *Fermi*-LAT data, a few times during 2011–2012 in the low-energy (0.2–2 GeV) as well as in the high-energy band (2–300 GeV; see Figure 4). The origin of this very hard spectrum is still under debate.

This work used results provided by the ASM/*RXTE* teams at MIT. This study also used *Swift*/BAT transient monitor results provided by the *Swift*/BAT team. This research has also made use of data obtained from the High Energy Astrophysics Science Archive Research Center (HEASARC), provided by NASA's Goddard Space Flight Center. Data from the Steward Observatory spectropolarimetric monitoring project used supported by *Fermi* Guest Investigator grants NNX08AW56G and NNX09AU10G. Radio data at 15 GHz are used from the OVRO 40 M Telescope, and this *Fermi* blazar monitoring program is supported by NASA under award NNX08AW31G and by the NSF under award 0808050. This research has made use of the XRT Data Analysis Software (XRTDAS) developed under the responsibility of the ASI Science Data Center (ASDC), Italy. We are grateful to the engineering and technical staff of IIA and TIFR, who have taken part in the construction of the HAGAR telescopes and contributed to the setting up of the front-end electronics and the data acquisition. We also thank Dr. David Paneque and Dr. Chen Songzhan for providing the published data of Mrk 501 to use in this study.

REFERENCES

Abdo, A. A., Ackermann, M., Ajello, M., et al. 2011, ApJ, 727, 129
Acciari, V. A., Arlen, T., Aune, T., et al. 2011, ApJ, 729, 2
Aharonian, F., Akhperjanian, A. G., Barrio, J. A., et al. 1999a, A&A, 349, 29
Aharonian, F., Akhperjanian, A., Barrio, J., et al. 2001, ApJ, 546, 898
Aharonian, F. A. 2000, NewA, 5, 377
Aharonian, F. A., Akhperjanian, A., Barrio, J., et al. 1999b, A&A, 342, 69
Albert, J., Aliu, E., Anderhub, H., et al. 2007, ApJ, 669, 862
Atwood, W. B., Abdo, A. A., Ackermann, M., et al. 2009, ApJ, 697, 1071
Bartoli, B., Bernardini, P., Bi, X. J., et al. 2012, ApJ, 758, 2
Begelman, M. C., Fabian, A. C., & Rees, M. J. 2008, MNRAS, 384, L19
Bradt, H. V., Rothschild, R. E., & Swank, J. H. 1993, A&AS, 97, 355
Burrows, D. N., Hill, J. E., Nousek, J. A., et al. 2005, SSRv, 120, 165
Cash, W. 1979, ApJ, 228, 939
Catanese, M., Bradbury, S. M., Breslin, A. C., et al. 1997, ApJL, 487, L143
Cerruti, M., Zech, A., Boisson, C., & Inoue, S. 2012, in AIP Conf. Ser. 1505, High Energy Gamma-Ray Astronomy: Fifth Intl. Mtg. High-energy Gamma-ray Astronomy, ed. F. A. Aharonian, W. Hofmann, & F. M. Rieger (Melville, NY: AIP), 635
Chitnis, V. R., Pendharkar, J. K., Bose, D., et al. 2009, ApJ, 698, 1207
Crusius-Waetzel, A. R., & Lesch, H. 1998, A&A, 338, 399
Dermer, C. D., & Schlickeiser, R. 1993, ApJ, 416, 458
Georganopoulos, M., & Kazanas, D. 2003, ApJL, 594, L27
Ghisellini, G., Celotti, A., & Costamante, L. 2002, A&A, 386, 833
Ghisellini, G., & Madau, P. 1996, MNRAS, 280, 67
Ghisellini, G., Tavecchio, F., Bodo, G., & Celotti, A. 2009, MNRAS, 393, L16
Ghisellini, G., Tavecchio, F., & Chiaberge, M. 2005, A&A, 432, 401
Giannios, D., Uzdensky, D. A., & Begelman, M. C. 2009, MNRAS, 395, L29
Giannios, D., Uzdensky, D. A., & Begelman, M. C. 2010, MNRAS, 402, 1649
Giroletti, M., Giovannini, G., Feretti, L., et al. 2004, ApJ, 600, 127
Gliozzi, M., Sambruna, R. M., Jung, I., et al. 2006, ApJ, 646, 61
Gothe, K. S., Prabhu, T. P., Vishwanath, P. R., et al. 2013, ExA, 35, 489
Graff, P. B., Georganopoulos, M., Perlman, E. S., & Kazanas, D. 2008, ApJ, 689, 68
Gupta, A. C., Deng, W. G., Joshi, U. C., Bai, J. M., & Lee, M. G. 2008, NewA, 13, 375
Gupta, S. P., Pandey, U. S., Singh, K., et al. 2012, NewA, 17, 8
Kalberla, P. M. W., Burton, W. B., Hartmann, D., et al. 2005, A&A, 440, 775
Katarzyński, K., Ghisellini, G., Tavecchio, F., Gracia, J., & Maraschi, L. 2006, MNRAS, 368, L52
Katarzyński, K., Sol, H., & Kus, A. 2001, A&A, 367, 809
Krawczynski, H. 2004, NewA, 48, 367
Krawczynski, H., Coppi, P. S., Maccarone, T., & Aharonian, F. A. 2000, A&A, 353, 97
Krawczynski, H., Hughes, S. B., Horan, D., et al. 2004, ApJ, 601, 151
Krimm, H. A., Holland, S. T., Corbet, R. H. D., et al. 2013, ApJS, 209, 14
Krishan, V., & Wiita, P. J. 1994, ApJ, 423, 172
Lefa, E., Aharonian, F. A., & Rieger, F. M. 2011a, ApJL, 743, L19
Lefa, E., Rieger, F. M., & Aharonian, F. 2011b, ApJ, 740, 64
Levinson, A. 2007, ApJL, 671, L29
Mannheim, K. 1998, Sci, 279, 684
Mattox, J. R., Bertsch, D. L., Chiang, J., et al. 1996, ApJ, 461, 396
Mücke, A., Protheroe, R. J., Engel, R., Rachen, J. P., & Stanev, T. 2003, APh, 18, 593
Neronov, A., Semikoz, D., & Taylor, A. M. 2012, A&A, 541, A31
Pian, E., Vacanti, G., Tagliaferri, G., et al. 1998, ApJL, 492, L17
Quinn, J., Akerlof, C. W., Biller, S., et al. 1996, ApJL, 456, L83
Richards, J. L., Max-Moerbeck, W., Pavlidou, V., et al. 2011, ApJS, 194, 29
Roming, P. W. A., Kennedy, T. E., Mason, K. O., et al. 2005, SSRv, 120, 95
Saha, L., Chitnis, V. R., Vishwanath, P. R., et al. 2013, APh, 42, 33
Sambruna, R. M., Aharonian, F. A., Krawczynski, H., et al. 2000, ApJ, 538, 127
Schlegel, D. J., Finkbeiner, D. P., & Davis, M. 1998, ApJ, 500, 525
Shukla, A., Chitnis, V. R., Vishwanath, P. R., et al. 2012, A&A, 541, A140
Smith, P. S., Montiel, E., Rightley, S., et al. 2009, arXiv:0912.3621
Subramanian, P., Shukla, A., & Becker, P. A. 2012, MNRAS, 423, 1707
Tavecchio, F., Ghisellini, G., Ghirlanda, G., Costamante, L., & Franceschini, A. 2009, MNRAS, 399, L59
Tavecchio, F., Maraschi, L., Pian, E., et al. 2001, ApJ, 554, 725
Villata, M., & Raiteri, C. M. 1999, A&A, 347, 30
Xue, Y., & Cui, W. 2005, ApJ, 622, 160